

A two-stage fourth order time-accurate discretization
for Lax–Wendroff type flow solvers
II. High order numerical boundary conditions

Zhifang Du^a, Jiequan Li^{b,*}

^a*School of Mathematical Sciences, Beijing Normal University, 100875, Beijing, P. R. China*

^b*Laboratory of Computational Physics, Institute of Applied Physics and Computational Mathematics, Beijing, P. R. China*

Abstract

This paper serves to treat boundary conditions numerically with high order accuracy in order to match the two-stage fourth-order finite volume schemes for hyperbolic problems developed in [*J. Li and Z. Du, A two-stage fourth order time-accurate discretization Lax–Wendroff type flow solvers, I. Hyperbolic conservation laws, SIAM, J. Sci. Comput., 38 (2016), pp. A3046–A3069*]. As such, it is significant when capturing small scale structures near physical boundaries. Different from previous contributions in literature, the current approach constructs a fourth order accurate approximation to boundary conditions by only using the Jacobian of the flux function (characteristic information) instead of its successive differentiation leading to tensors of high ranks in the inverse Lax–Wendroff method. Technically, data in several ghost cells are constructed with HWENO interpolation so that the interior scheme can be implemented over boundary cells, and theoretical boundary condition has to be modified properly at intermediate stages so as to make the two-stage scheme over boundary cells fully consistent with that over interior cells. This highlights the fact that *continuous boundary conditions only match continuous partial differential equations (PDEs), and they must be approximated in a consistent way (even though*

*Corresponding author

Email addresses: du@mail.bnu.edu.cn (Zhifang Du), li_jiequan@iapcm.ac.cn (Jiequan Li)

it could be exactly valued) when the PDEs are discretized. Several numerical examples are provided to illustrate the performance of the current approach when dealing with general boundary conditions.

Keywords: hyperbolic conservation laws, two-stage fourth-order accurate scheme, Lax-Wendroff type flow solvers, Fourth order numerical boundary conditions

2010 MSC: 65M08, 76M12, 35L60, 35L65, 76N15

1. Introduction

This study aims to develop high order accurate numerical approximations to theoretical boundary conditions suitable for the two-stage fourth-order accurate finite volume scheme based on the Lax–Wendroff type flow solvers in [12]. This scheme distinguishes from the Runge–Kutta type schemes in the sense that second-order Lax–Wendroff type flow solvers [12, 15] are used to achieve fourth-order temporal accuracy through two-stage temporal iterations. The numerical evidence shows that it is less computational consuming, less dissipative near discontinuities and more effective to capture the physical and the multi-dimensional effects. Yet, the numerical boundary conditions have not been constructed correspondingly and in particular, the theoretical boundary data have to be modified at intermediate stages, analogous to many other multi-stage methods [4, 16].

There are a large number of contributions to numerical boundary conditions for hyperbolic problems in literature and most of them are only first- or second-order accurate. For example, second-order accurate finite difference approximations are constructed for the wave equation with Dirichlet or Neumann boundary conditions in [9, 10] from which our basic idea comes. As is well-known, a second order wave equation is equivalent to a system of first order hyperbolic equations. Therefore the similar idea applies for a boundary treatment of hyperbolic conservation laws in [18]. We briefly illustrate their

idea in the finite difference framework by considering the initial boundary value problem (IBVP) for a scalar conservation law

$$\begin{cases} \frac{\partial u}{\partial t} + \frac{\partial f(u)}{\partial x} = 0, & x \in (0, 1), t > 0, \\ u(x, 0) = u_0(x), & x \in (0, 1), \\ u(0, t) = g(t), & t > 0. \end{cases} \quad (1)$$

Assume that $f'(u) > 0$ for all $u \in \mathbb{R}$ so $x = 0$ is an inflow boundary and $x = 1$ is an outflow boundary. We equally distribute $M + 1$ points $\{x_j = (j - 1/2)h : j = 0, 1, \dots, M\}$ in the computational domain $(0, 1)$, as shown in Figure 1. Obviously at the inflow boundary, the solution value at the ghost point x_{-1}

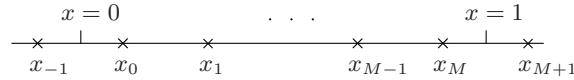


Figure 1: The computational domain. Set $x_0 = h/2$ and $x_M = 1 - h/2$. $x_{-1} = -h/2$ and $x_{M+1} = 1 + h/2$ are ghost points.

is required in order to perform a second-order finite difference at x_0 . For this purpose, we construct a polynomial in the region around the inflow boundary by using the pointwise values u_{-1} , u_0 and u_1 ,

$$L(x) = g_{-1}(x)u_{-1} + g_0(x)u_0 + g_1(x)u_1, \quad (2)$$

from which we want to find the value u_{-1} . The Lagrangian interpolation tells that

$$g_{-1}(x) = \frac{(x - x_0)(x - x_1)}{2h^2}, \quad g_0(x) = \frac{(x - x_{-1})(x - x_1)}{-h^2}, \quad g_1(x) = \frac{(x - x_{-1})(x - x_0)}{2h^2}. \quad (3)$$

Then we can get u_{-1} by solving the linear equation $u(0, t) = L(0)$ where $u(0, t) = g(t)$. At the outflow boundary $x = 1$, simply use the extrapolation

$$u_{M+1} = 2u_M - u_{M-1} \quad (4)$$

to obtain the value u_{M+1} since the signal goes out of the computational domain at this end. Other works can be found on first- and second-order accurate

approaches for hyperbolic conservation laws in the finite volume framework in, e.g. [3, 6, 5] and on the body fitted boundary treatment for the discontinuous Galerkin (DG) methods in [11] which takes the advantage of the compactness.

In the present paper, we propose a fourth-order accurate boundary treatment for the two-stage fourth-order finite volume scheme developed in [12]. This boundary treatment can be regarded as a fourth-order extension of the methods developed in [9, 10, 18]. With the methodology described above, a polynomial is constructed near the boundary to interpolate the data in ghost cells with the information from both the interior cells and the boundary condition $u(0, t) = g(t)$. In order to reduce the number of the interior cells used, first-order spatial derivatives of the conservative variables are utilized in addition to their values at the boundary, for which we adopt the inverse Lax-Wendroff approach in [7, 22, 19, 20, 13]. The novelty here is the governing equations are just used once in the process of the substitution of spatial derivatives by temporal derivatives rather than used repeatedly, avoiding the complexity caused by successive differentiation of flux vector functions. Moreover, in analogy with other multi-stage methods [4, 16], the theoretical boundary data needs modifying properly at the intermediate stage so that fourth order accuracy is achieved. Certainly, a WENO type stencil selection procedure is taken to suppress possible oscillations when discontinuities are present close to boundaries.

This paper is organized as follows. After the introduction section, we will have a brief review over the two-stage fourth-order scheme for hyperbolic conservation laws in Section 2. In Section 3, the basic idea and formulation are explained using the one-dimensional scalar equation. The system case is shown in Section 4. The results of several numerical examples are shown in Section 5 to show the validity of the current numerical boundary treatment.

2. A review over the two-stage fourth-order scheme

In [12], we proposed a two-stage fourth order accurate temporal discretization based on Lax–Wendroff type flow solvers, particularly for hyperbolic conservation laws,

$$\frac{\partial \mathbf{u}}{\partial t} + \frac{\partial \mathbf{f}(\mathbf{u})}{\partial x} = 0, \quad x \in \mathbb{R}, t > 0, \quad (5)$$

$$\mathbf{u}(x, 0) = \mathbf{u}_0(x), \quad x \in \mathbb{R},$$

where \mathbf{u} is a conservative variable and $\mathbf{f}(\mathbf{u})$ is the associated flux function vector. Given a computational mesh $I_j = (x_{j-\frac{1}{2}}, x_{j+\frac{1}{2}})$ with center at $x_j = \frac{1}{2}(x_{j-\frac{1}{2}} + x_{j+\frac{1}{2}})$ and the size $h_j = x_{j+\frac{1}{2}} - x_{j-\frac{1}{2}}$. Then we write (5) in form of the balance law,

$$\frac{d\bar{\mathbf{u}}_j(t)}{dt} = \mathcal{L}_j(\mathbf{u}) := -\frac{1}{h_j}[\mathbf{f}(\mathbf{u}(x_{j+\frac{1}{2}}, t)) - \mathbf{f}(\mathbf{u}(x_{j-\frac{1}{2}}, t))], \quad (6)$$

where $\bar{\mathbf{u}}_j(t)$ is the average of the solution $\mathbf{u}(x, t)$ over the control volume I_j ,

$$\bar{\mathbf{u}}_j(t) = \frac{1}{h_j} \int_{I_j} \mathbf{u}(x, t) dt, \quad (7)$$

and $\mathbf{u}(x_{j+\frac{1}{2}}, t)$ is the solution of (6) in a certain sense. Thanks to the Lax–Wendroff flow solvers, which is specialized as the GRP solver [2] in the current study, $\mathcal{L}_j(\mathbf{u})$ is well-defined. Then the two-stage approach for (5) is summarized as follows.

Step 1. With the initial data $\mathbf{u}(x, t^n) = \mathbf{u}^n(x)$ obtained by the Hermite-type WENO interpolation [17], we compute the Riemann solutions $\mathbf{u}_{j+\frac{1}{2}}^n$ and the GRP solutions $(\partial \mathbf{u} / \partial t)_{j+\frac{1}{2}}^n$ using the GRP solver [2].

Step 2. Compute the intermediate cell averages $\bar{\mathbf{u}}^{n+\frac{1}{2}}(x)$ at $t^{n+\frac{1}{2}} = t^n + \frac{k}{2}$ using the formulae,

$$\begin{aligned} \bar{\mathbf{u}}_j^{n+\frac{1}{2}} &= \bar{\mathbf{u}}_j^n - \frac{k}{2h}[\mathbf{f}_{j+\frac{1}{2}}^* - \mathbf{f}_{j-\frac{1}{2}}^*], \\ \mathbf{f}_{j+\frac{1}{2}}^* &= \mathbf{f}(\mathbf{u}_{j+\frac{1}{2}}^n) + \frac{k}{4} \frac{\partial \mathbf{f}}{\partial \mathbf{u}}(\mathbf{u}_{j+\frac{1}{2}}^n) \left(\frac{\partial \mathbf{u}}{\partial t} \right)_{j+\frac{1}{2}}^n, \end{aligned} \quad (8)$$

where k is the time step size constrained by the CFL condition, and $\partial \mathbf{f} / \partial \mathbf{u}$ is the Jacobian of $\mathbf{f}(\mathbf{u})$. Then we use the Hermite-type WENO interpolation

again to construct a piecewise polynomial $\mathbf{u}^{n+\frac{1}{2}}(x)$ and continue to find the GRP solutions $\mathbf{u}_{j+\frac{1}{2}}^{n+\frac{1}{2}}$ and $(\partial\mathbf{u}/\partial t)_{j+\frac{1}{2}}^{n+\frac{1}{2}}$ at the stage $t^{n+\frac{1}{2}} = t^n + \frac{k}{2}$, as was done in Step 1.

Step 3. Advance the solution to the next time level $t^{n+1} = t^n + k$,

$$\begin{aligned}\bar{\mathbf{u}}_j^{n+1} &= \bar{\mathbf{u}}_j^n - \frac{k}{h}[\mathbf{f}_{j+\frac{1}{2}}^{4th} - \mathbf{f}_{j-\frac{1}{2}}^{4th}], \\ \mathbf{f}_{j+\frac{1}{2}}^{4th} &= \mathbf{f}(\mathbf{u}_{j+\frac{1}{2}}^n) + \frac{k}{2} \left[\frac{1}{3} \frac{\partial \mathbf{f}}{\partial \mathbf{u}}(\mathbf{u}_{j+\frac{1}{2}}^n) \left(\frac{\partial \mathbf{u}}{\partial t} \right)_{j+\frac{1}{2}}^n + \frac{2}{3} \frac{\partial \mathbf{f}}{\partial \mathbf{u}}(\mathbf{u}_{j+\frac{1}{2}}^{n+1/2}) \left(\frac{\partial \mathbf{u}}{\partial t} \right)_{j+\frac{1}{2}}^{n+1/2} \right],\end{aligned}\tag{9}$$

where $\mathbf{f}_{j+\frac{1}{2}}^{4th}$ is the fourth order numerical flux.

In this approach, the Hermite-type WENO reconstruction [17] is used to achieve a high order accuracy in space. Given the cell averages $\bar{\mathbf{u}}_j$ and the x -differences $\Delta\mathbf{u}_j$ of the solution \mathbf{u} ,

$$\bar{\mathbf{u}}_j = \frac{1}{h_j} \int_{I_j} \mathbf{u}(x, t) dx, \quad \Delta\mathbf{u}_j = \frac{1}{h} \int_{I_j} \mathbf{u}_x(x, t) dx = \frac{1}{h} \left(\mathbf{u}(x_{j+\frac{1}{2}, -}, t) - \mathbf{u}(x_{j-\frac{1}{2}, +}, t) \right),\tag{10}$$

the cell boundary values are reconstructed as

$$\begin{aligned}\mathbf{u}_{j-\frac{1}{2}, -} &= \frac{1}{120}(-23\bar{\mathbf{u}}_{j-2} + 76\bar{\mathbf{u}}_{j-1} + 67\bar{\mathbf{u}}_j - 9h\Delta\mathbf{u}_{j-2} - 21h\Delta\mathbf{u}_j), \\ \mathbf{u}_{j-\frac{1}{2}, +} &= \frac{1}{120}(67\bar{\mathbf{u}}_{j-1} + 76\bar{\mathbf{u}}_j - 23\bar{\mathbf{u}}_{j+1} + 21h\Delta\mathbf{u}_{j-1} + 9h\Delta\mathbf{u}_{j+1}), \\ (\partial\mathbf{u}/\partial x)_{j-\frac{1}{2}, \pm} &= \frac{1}{12h}(\bar{\mathbf{u}}_{j-2} - 15\bar{\mathbf{u}}_{j-1} + 15\bar{\mathbf{u}}_j - \bar{\mathbf{u}}_{j+1}).\end{aligned}\tag{11}$$

In the presence of discontinuities, a WENO-type stencil selection is performed. Details can be found in [17].

Remark 2.1. *The Riemann solutions $\mathbf{u}_{j+\frac{1}{2}}^n$, and the GRP solutions $(\partial\mathbf{u}/\partial t)_{j+\frac{1}{2}}^n$ in Step 1 are defined as*

$$\begin{aligned}\mathbf{u}_{j+\frac{1}{2}}^n &= \lim_{t \rightarrow t^n+0} \mathbf{u}(x_{j+\frac{1}{2}}, t), \\ \left(\frac{\partial \mathbf{u}}{\partial t} \right)_{j+\frac{1}{2}}^n &= \lim_{t \rightarrow t^n+0} \frac{\partial \mathbf{u}}{\partial t}(x_{j+\frac{1}{2}}, t) = \lim_{t \rightarrow t^n+0} -\frac{\partial \mathbf{f}}{\partial \mathbf{u}}(\mathbf{u}(x_{j+\frac{1}{2}}, t)) \frac{\partial \mathbf{u}}{\partial x}(x_{j+\frac{1}{2}}, t).\end{aligned}\tag{12}$$

The last equality explains the Lax-Wendroff methodology for which the governing equation (5) is employed. In practice, due to the discontinuity of the initial data

$\mathbf{u}^n(x)$ at $(x_{j+\frac{1}{2}}, t^n)$, the GRP solver is applied to resolve the singularity and both values $\mathbf{u}_{j+\frac{1}{2}}^{n+\frac{1}{2}}$ and $(\partial\mathbf{u}/\partial t)_{j+\frac{1}{2}}^{n+\frac{1}{2}}$ are defined.

In [12], we did not touch the indispensable numerical boundary conditions. In the coming sections, we will present numerical boundary conditions suitable for the implementation of this two-stage scheme.

3. One-dimensional numerical boundary treatment for scalar conservation laws

Let's consider (5) in the computational domain $(0, 1)$ and assume that $\mathbf{f}(\mathbf{u})$ to be scalar $\mathbf{f}(\mathbf{u}) = f(u)$ with $f'(u) > 0$ for any value of $u \in \mathbb{R}$. Then $x = 0$ is an inflow boundary and $x = 1$ is an outflow boundary. Thus a boundary condition is required at $x = 0$. Denote by $u(0, t) = g(t)$ the boundary condition for $t > 0$. The resulting initial boundary value problem (IBVP) can be formulated as in (1). The mesh $\{I_j = (x_{j-\frac{1}{2}}, x_{j+\frac{1}{2}}) : x_{j-\frac{1}{2}} = jh, j = 0, 1, \dots, M\}$ is used in the computation. Notice that in order to place the left boundary at $x = 0$, our mesh is a little different from $I_j = ((j-1/2)h, (j+1/2)h)$ that is conventionally used in the finite volume context.

In the numerical computations, we need numerical boundary conditions at the inflow boundary $x = 0$ corresponding to the boundary condition $\mathbf{u}(0, t) = g(t), t > 0$. In this section, we will formulate the numerical treatment for the inflow boundary conditions and present the modification at the intermediate stages. The WENO-type extrapolation is introduced to deal with the outflow boundary conditions in the last part of this section, which is the same as that in [20].

3.1. Inflow boundary condition

As far as the IBVP (1) is concerned with, several values outside of the computational domain are needed. For the present case, $\bar{u}_{-1}, \bar{u}_{-2}, \Delta u_{-1}$ and Δu_{-2} are needed in the reconstruction procedure (11) for the values indexed by $j = 0$

and $j = 1$. We call I_{-1} and I_{-2} ghost cells. In this subsection, we suppress all superscripts just for the simplicity of presentation.

First of all, assume the solution to be smooth near the boundary $x = 0$. To obtain the values mentioned above, a cubic polynomial,

$$p(x) = \alpha_3 x^3 + \alpha_2 x^2 + \alpha_1 x + \alpha_0, \quad (13)$$

is constructed over $I_{-2} \cup I_{-1} \cup I_0 \cup I_1 = (-2h, 2h)$ to interpolate the solution $u(x, t^n)$ such that

$$\frac{1}{h} \int_{I_i} p(x) dx = \bar{u}_i, \quad i = -2, -1, 0, 1. \quad (14)$$

Substitute the constraints (14) into (13) to determine the coefficients $\alpha_0, \alpha_1, \alpha_2$ and α_3 as

$$\begin{aligned} \alpha_3 &= \frac{\bar{u}_1 - 3\bar{u}_0 + 3\bar{u}_{-1} - \bar{u}_{-2}}{6h^3}, & \alpha_2 &= \frac{\bar{u}_1 - \bar{u}_0 - \bar{u}_{-1} + \bar{u}_{-2}}{4h^2}, \\ \alpha_1 &= \frac{-\bar{u}_1 + 15\bar{u}_0 - 15\bar{u}_{-1} + \bar{u}_{-2}}{12h}, & \alpha_0 &= \frac{-\bar{u}_1 + 7\bar{u}_0 + 7\bar{u}_{-1} - \bar{u}_{-2}}{12}, \end{aligned} \quad (15)$$

in which \bar{u}_{-1}^n and \bar{u}_{-2}^n are yet to be determined and they are obtained by evaluating $p(0)$ and $p'(0)$ at the boundary $x = 0$,

$$\begin{aligned} p(0) &= \frac{1}{12}(-\bar{u}_1 + 7\bar{u}_0 + 7\bar{u}_{-1} - \bar{u}_{-2}) = g(t) + \mathcal{O}(h^4), \\ p'(0) &= \frac{1}{12h}(-\bar{u}_1 + 15\bar{u}_0 - 15\bar{u}_{-1} + \bar{u}_{-2}) = -f'(g(t))^{-1} g'(t) + \mathcal{O}(h^3). \end{aligned} \quad (16)$$

The first equality results directly from the boundary condition $u(0, t) = g(t)$ and the interpolation accuracy $p(0) = u(0, t) + \mathcal{O}(h^4)$; the second one is obtained by using the inverse Lax-Wendroff approach that expresses the spatial variation through the temporal variation. Solving (16) in terms of \bar{u}_{-1} and \bar{u}_{-2} yields (by ignoring high order terms)

$$\begin{aligned} \bar{u}_{-1} &= \frac{1}{4}(-6g + 6h f'(g)^{-1} g' + 11\bar{u}_0 - \bar{u}_1), \\ \bar{u}_{-2} &= \frac{1}{4}(-90g + 42h f'(g)^{-1} g' + 105\bar{u}_0 - 11\bar{u}_1). \end{aligned} \quad (17)$$

Substituting (17) into (15), in turn, gives us the explicit expressions of α_i , $i = 0, \dots, 3$, and then the expression of $p(x)$. Therefore we have (by ignoring

high order terms)

$$\begin{aligned}
\Delta u_{-1} &= \frac{1}{h} (p(0) - p(-h)) \\
&= \frac{1}{8h} (66g - 34 h f'(g)^{-1} g' - 73\bar{u}_0 + 7\bar{u}_1), \\
\Delta u_{-2} &= \frac{1}{h} (p(-h) - p(-2h)) \\
&= \frac{1}{8h} (294g - 118 h f'(g)^{-1} g' - 331\bar{u}_0 + 37\bar{u}_1).
\end{aligned} \tag{18}$$

The truncation errors of the above approximations are of order $\mathcal{O}(h^3)$ due to the accuracy of $p(x)$. Thus (17) and (18) together provide the values in the ghost cells.

As there are discontinuities close to the inflow boundary, a WENO-type stencil selecting procedure can be applied. Assume that there is a discontinuity in either I_0 or I_1 , we shorten the stencil cell by cell. Denote the stencils by

$$S^{(2)} = \{I_{-2}, I_{-1}, I_0, I_1\}, \quad S^{(1)} = \{I_{-2}, I_{-1}, I_0\}, \quad S^{(0)} = \{I_{-2}, I_{-1}\}. \tag{19}$$

Denote by $p^{(r)}(x)$ the polynomial on $S^{(r)}$, $r = 0, 1, 2$, just as the polynomial $p(x)$ constructed before. Then define

$$\begin{aligned}
\bar{u}_{-1}^{(r)} &= \frac{1}{h} \int_{I_{-1}} p^{(r)}(x) dx, & \bar{u}_{-2}^{(r)} &= \frac{1}{h} \int_{I_{-2}} p^{(r)}(x) dx, \\
\Delta u_{-1}^{(r)} &= \frac{1}{h} (p^{(r)}(0) - p^{(r)}(-h)), & \Delta u_{-2}^{(r)} &= \frac{1}{h} (p^{(r)}(-h) - p^{(r)}(-2h)).
\end{aligned} \tag{20}$$

The expressions of $\bar{u}_{-1}^{(r)}$, $\bar{u}_{-2}^{(r)}$, $\Delta u_{-1}^{(r)}$ and $\Delta u_{-2}^{(r)}$ for $r = 0, 1, 2$ will be listed in Appendix A.1.

The smoothness indicators are defined in the same way as for the classical WENO interpolation,

$$\beta^{(r)} = \sum_{l=1}^{\infty} \int_{I_{-1}} h^{2l-1} \left(\frac{d^l p^{(r)}}{dx^l} \right)^2 dx, \tag{21}$$

where $p^{(r)}$ is the interpolation polynomial in the stencil $S^{(r)}$. Expressions of $\beta^{(r)}$ are put in Appendix A.2. With the Taylor expansion, we can express them at

the boundary as

$$\begin{aligned}
\beta^{(2)} &= h^2 \left(\frac{\partial u}{\partial x} \right)^2 - h^3 \frac{\partial u}{\partial x} \frac{\partial^2 u}{\partial x^2} + h^4 \left[\frac{4}{3} \left(\frac{\partial^2 u}{\partial x^2} \right)^2 + \frac{1}{3} \frac{\partial u}{\partial x} \frac{\partial^3 u}{\partial x^3} \right] + \mathcal{O}(h^5), \\
\beta^{(1)} &= h^2 \left(\frac{\partial u}{\partial x} \right)^2 - h^3 \frac{\partial u}{\partial x} \frac{\partial^2 u}{\partial x^2} + h^4 \left[\frac{4}{3} \left(\frac{\partial^2 u}{\partial x^2} \right)^2 - \frac{1}{4} \frac{\partial u}{\partial x} \frac{\partial^3 u}{\partial x^3} \right] + \mathcal{O}(h^5), \\
\beta^{(0)} &= h^2,
\end{aligned} \tag{22}$$

where $\partial u/\partial x$, $\partial^2 u/\partial x^2$ and $\partial^3 u/\partial x^3$ are evaluated at $x = 0$. Actually $\beta^{(0)}$ should be $h^2(\partial u/\partial x)^2$ following the definition (21). However, in the practice, it would cause some instabilities while the choice of h^2 is fine. The linear weights of each stencil are

$$d^{(0)} = h^2, \quad d^{(1)} = h, \quad d^{(2)} = 1 - d^{(0)} - d^{(1)}. \tag{23}$$

Then, we calculate the weights of the stencils by

$$\alpha^{(r)} = \frac{d^{(r)}}{(\varepsilon + \beta^{(r)})^2}, \quad \omega^{(r)} = \frac{\alpha^{(r)}}{\sum \alpha^{(l)}}. \tag{24}$$

Finally, we obtain

$$\begin{aligned}
\bar{u}_{-1} &= \sum_{r=0}^2 \omega^{(r)} \bar{u}_{-1}^{(r)}, & \bar{u}_{-2} &= \sum_{r=0}^2 \omega^{(r)} \bar{u}_{-2}^{(r)}, \\
\Delta u_{-1} &= \sum_{r=0}^2 \omega^{(r)} \Delta u_{-1}^{(r)}, & \Delta u_{-2} &= \sum_{r=0}^2 \omega^{(r)} \Delta u_{-2}^{(r)}.
\end{aligned} \tag{25}$$

3.2. Inflow boundary treatment at intermediate stages

As pointed out by many researchers e.g., in [4, 16], the direct use of exact boundary conditions at the intermediate stages in the process of multi-stage time discretizations will cause defects of the numerical accuracy. The same argument applies in the current study. We need to treat the boundary condition properly at the intermediate stage.

Our strategy is made as follows. First, expand the advancing formula of the two-stage fourth-order accurate scheme in (9) for the left boundary control

volume, for which $j = 0$, as

$$\begin{aligned}
u_0^{n+1} &= \bar{u}_0^n - \frac{k}{h} \left[f_{\frac{1}{2}}^{4th} - f_{-\frac{1}{2}}^{4th} \right] \\
&= \bar{u}_0^n - \frac{1}{h} \left\{ k \left[f(u_{\frac{1}{2}}^n) - f(u_{-\frac{1}{2}}^n) \right] \right. \\
&\quad + \frac{k^2}{6} \left[f'(u_{\frac{1}{2}}^n) \left(\frac{\partial u}{\partial t} \right)_{\frac{1}{2}}^n - f'(u_{-\frac{1}{2}}^n) \left(\frac{\partial u}{\partial t} \right)_{-\frac{1}{2}}^n \right] \\
&\quad \left. + \frac{k^2}{3} \left[f'(u_{\frac{1}{2}}^{n+\frac{1}{2}}) \left(\frac{\partial u}{\partial t} \right)_{\frac{1}{2}}^{n+\frac{1}{2}} - f'(u_{-\frac{1}{2}}^{n+\frac{1}{2}}) \left(\frac{\partial u}{\partial t} \right)_{-\frac{1}{2}}^{n+\frac{1}{2}} \right] \right\} \\
&= \bar{u}_0^n - \frac{1}{h} \left\{ k \left[f(u_{\frac{1}{2}}^n) - f(u_{-\frac{1}{2}}^n) \right] \right. \\
&\quad - \frac{k^2}{6} \left[(f'(u_{\frac{1}{2}}^n))^2 \left(\frac{\partial u}{\partial x} \right)_{\frac{1}{2}}^n - (f'(u_{-\frac{1}{2}}^n))^2 \left(\frac{\partial u}{\partial x} \right)_{-\frac{1}{2}}^n \right] \\
&\quad \left. - \frac{k^2}{3} \left[(f'(u_{\frac{1}{2}}^{n+\frac{1}{2}}))^2 \left(\frac{\partial u}{\partial x} \right)_{\frac{1}{2}}^{n+\frac{1}{2}} - (f'(u_{-\frac{1}{2}}^{n+\frac{1}{2}}))^2 \left(\frac{\partial u}{\partial x} \right)_{-\frac{1}{2}}^{n+\frac{1}{2}} \right] \right\}, \tag{26}
\end{aligned}$$

where the temporal derivatives are replaced by the spatial derivatives in the last equality. The difficulty results from the presence of $(\partial u / \partial x)_{\frac{1}{2}}^{n+\frac{1}{2}}$ and $(\partial u / \partial x)_{-\frac{1}{2}}^{n+\frac{1}{2}}$ evaluated at the intermediate stage. In fact, the interpolation are stated in (11) and specified to this boundary volume as,

$$\begin{aligned}
\left(\frac{\partial u}{\partial x} \right)_{-\frac{1}{2}}^{n+\frac{1}{2}} &= \frac{1}{12h} (\bar{u}_{-2}^{n+\frac{1}{2}} - 15\bar{u}_{-1}^{n+\frac{1}{2}} + 15\bar{u}_0^{n+\frac{1}{2}} - \bar{u}_1^{n+\frac{1}{2}}), \\
\left(\frac{\partial u}{\partial x} \right)_{\frac{1}{2}}^{n+\frac{1}{2}} &= \frac{1}{12h} (\bar{u}_{-1}^{n+\frac{1}{2}} - 15\bar{u}_0^{n+\frac{1}{2}} + 15\bar{u}_1^{n+\frac{1}{2}} - \bar{u}_2^{n+\frac{1}{2}}), \tag{27}
\end{aligned}$$

where $\bar{u}_{-1}^{n+\frac{1}{2}}$ and $\bar{u}_{-2}^{n+\frac{1}{2}}$ are determined in (17). Substituting (17) into (27) gives their direct reconstructions

$$\begin{aligned}
\left(\frac{\partial u}{\partial x} \right)_{-\frac{1}{2}}^{n+\frac{1}{2}} &= -(f'(g(t^{n+\frac{1}{2}})))^{-1} g'(t^{n+\frac{1}{2}}), \\
\left(\frac{\partial u}{\partial x} \right)_{\frac{1}{2}}^{n+\frac{1}{2}} &= \frac{1}{48h} \left[-49\bar{u}_0^{n+\frac{1}{2}} + 59\bar{u}_1^{n+\frac{1}{2}} - 4\bar{u}_2^{n+\frac{1}{2}} \right. \\
&\quad \left. - 6g(t^{n+\frac{1}{2}}) + 6h(f'(g(t^{n+\frac{1}{2}})))^{-1} g'(t^{n+\frac{1}{2}}) \right]. \tag{28}
\end{aligned}$$

The errors in the above formulae come from two sources: the interpolation error and the truncation error carried by $\bar{u}_0^{n+\frac{1}{2}}$, $\bar{u}_1^{n+\frac{1}{2}}$ and $\bar{u}_2^{n+\frac{1}{2}}$ within second-order accuracy. The latter one can be analyzed carefully as follows.

Recall the calculation of the intermediate state in the two-stage fourth-order scheme in (8) and a second-order approximation to the flux $f_{j+\frac{1}{2}}^*$,

$$\begin{aligned} \frac{k}{2}f_{j+\frac{1}{2}}^* &= \frac{k}{2}f(u_{j+\frac{1}{2}}^n) + \frac{k^2}{8}\left(\frac{\partial f}{\partial t}\right)_{j+\frac{1}{2}}^n \\ &= \int_{t^n}^{t^{n+\frac{1}{2}}} f(u(x_{j+\frac{1}{2}}, t))dt - \frac{k^3}{48}\frac{\partial^2 f}{\partial t^2}(x_{j+\frac{1}{2}}, t^n) + \mathcal{O}(k^4). \end{aligned} \quad (29)$$

This makes the intermediate value $\bar{u}_j^{n+\frac{1}{2}}$ in (28) bear truncation errors of order $\mathcal{O}(k^3)$,

$$\begin{aligned} \bar{u}_j^{n+\frac{1}{2}} &= \bar{u}_j^n - \frac{k}{2h}\left(f_{j+\frac{1}{2}}^{n+\frac{1}{2}} - f_{j-\frac{1}{2}}^{n+\frac{1}{2}}\right) \\ &= \bar{u}_j^n - \frac{1}{h}\left[\int_{t^n}^{t^{n+\frac{1}{2}}} f(u(x_{j+\frac{1}{2}}, t))dt - \frac{k^3}{48}\frac{\partial^2 f}{\partial t^2}(x_{j+\frac{1}{2}}, t^n) \right. \\ &\quad \left. - \int_{t^n}^{t^{n+\frac{1}{2}}} f(u(x_{j-\frac{1}{2}}, t))dt + \frac{k^3}{48}\frac{\partial^2 f}{\partial t^2}(x_{j-\frac{1}{2}}, t^n) + \mathcal{O}(k^5)\right] \\ &= \frac{1}{h}\int_{I_j} u(x, t^{n+\frac{1}{2}})dx + \frac{k^3}{48h}\left[\frac{\partial^2 f}{\partial t^2}(x_{j+\frac{1}{2}}, t^n) - \frac{\partial^2 f}{\partial t^2}(x_{j-\frac{1}{2}}, t^n)\right] + \mathcal{O}(k^4), \end{aligned} \quad (30)$$

where the difference in the bracket provides an $\mathcal{O}(h)$ term. This approximation can even tell more if replacing the difference by the differential quotient at $x = 0$, as specified to the boundary cells $j = 0, 1, 2$,

$$\bar{u}_j^{n+\frac{1}{2}} = \frac{1}{h}\int_{I_j} u(x, t^{n+\frac{1}{2}})dx + \frac{k^3}{48}\frac{\partial^3 f}{\partial t^2 \partial x}(0, t^n) + \mathcal{O}(k^4). \quad (31)$$

Then we use the inverse Lax–Wendroff approach replacing the spatial derivative by the corresponding temporal derivative through the governing equation (1)

$$\begin{aligned} \bar{u}_j^{n+\frac{1}{2}} &= \frac{1}{h}\int_{I_j} u(x, t^{n+\frac{1}{2}})dx - \frac{k^3}{48}\frac{\partial^3 u}{\partial t^3}(0, t^n) + \mathcal{O}(k^4) \\ &= \frac{1}{h}\int_{I_j} u(x, t^{n+\frac{1}{2}})dx - \frac{k^3}{48}g'''(t^n) + \mathcal{O}(k^4) \\ &= \frac{1}{h}\int_{I_j} u(x, t^{n+\frac{1}{2}})dx - \frac{k^3}{48}g'''(t^{n+\frac{1}{2}}) + \mathcal{O}(k^4). \end{aligned} \quad (32)$$

In order to eliminate the errors in (28) induced from (32), we use the follow-

ing formulae

$$\begin{aligned}
\left(\frac{\partial u}{\partial x}\right)_{-\frac{1}{2}}^{n+\frac{1}{2}} &= -(f'(g(t^{n+\frac{1}{2}})))^{-1}(g')^{n+\frac{1}{2}}, \\
\left(\frac{\partial u}{\partial x}\right)_{\frac{1}{2}}^{n+\frac{1}{2}} &= \frac{1}{48h} \left[-49\bar{u}_0^{n+\frac{1}{2}} + 59\bar{u}_1^{n+\frac{1}{2}} - 4\bar{u}_2^{n+\frac{1}{2}} \right. \\
&\quad \left. -6g^{n+\frac{1}{2}} + 6h(f'(g(t^{n+\frac{1}{2}})))^{-1}(g')^{n+\frac{1}{2}} \right].
\end{aligned} \tag{33}$$

to reconstruct $\left(\frac{\partial u}{\partial x}\right)_{\pm\frac{1}{2}}^{n+\frac{1}{2}}$ instead of the formulae in (28). Here the exact boundary values $g(t^{n+\frac{1}{2}})$ and $g'(t^{n+\frac{1}{2}})$ are replaced by

$$\begin{aligned}
g^{n+\frac{1}{2}} &= g(t^{n+\frac{1}{2}}) + e^{(0)}k^3, \\
(g')^{n+\frac{1}{2}} &= g'(t^{n+\frac{1}{2}}) + e^{(1)}k^2.
\end{aligned} \tag{34}$$

The errors $e^{(0)}k^3$ and $e^{(1)}k^2$ are introduced into $g^{n+\frac{1}{2}}$ and $(g')^{n+\frac{1}{2}}$ to cancel the errors in $\bar{u}_0^{n+\frac{1}{2}}$, $\bar{u}_1^{n+\frac{1}{2}}$ and $\bar{u}_2^{n+\frac{1}{2}}$. By combining (32), (33) and (34), we have

$$\begin{aligned}
\left(\frac{\partial u}{\partial x}\right)_{-\frac{1}{2}}^{n+\frac{1}{2}} &= -(f'(g(t^{n+\frac{1}{2}})))^{-1}(g')^{n+\frac{1}{2}} \\
&= -(f'(g(t^{n+\frac{1}{2}})))^{-1}g'(t^{n+\frac{1}{2}}) - (f'(g(t^{n+\frac{1}{2}})))^{-1}e^{(1)}k^2 \\
&= \frac{\partial u}{\partial x}(x_{-\frac{1}{2}}, t^{n+\frac{1}{2}}) - (f'(g(t^{n+\frac{1}{2}})))^{-1}e^{(1)}k^2,
\end{aligned} \tag{35}$$

and

$$\begin{aligned}
\left(\frac{\partial u}{\partial x}\right)_{\frac{1}{2}}^{n+\frac{1}{2}} &= \frac{1}{48h} \left[-49\bar{u}_0^{n+\frac{1}{2}} + 59\bar{u}_1^{n+\frac{1}{2}} - 4\bar{u}_2^{n+\frac{1}{2}} \right. \\
&\quad \left. -6g^{n+\frac{1}{2}} + 6h(f'(g(t^{n+\frac{1}{2}})))^{-1}(g')^{n+\frac{1}{2}} \right] \\
&= \frac{1}{48h} \left[-49\overline{u(\cdot, t^{n+\frac{1}{2}})}_0 + 59\overline{u(\cdot, t^{n+\frac{1}{2}})}_1 - 4\overline{u(\cdot, t^{n+\frac{1}{2}})}_2 \right. \\
&\quad \left. -6g(t^{n+\frac{1}{2}}) + 6h(f'(g(t^{n+\frac{1}{2}})))^{-1}g'(t^{n+\frac{1}{2}}) \right. \\
&\quad \left. - \frac{6}{48}k^3g'''(t^{n+\frac{1}{2}}) - 6e^{(0)}k^3 + 6(f'(g(t^{n+\frac{1}{2}})))^{-1}e^{(1)}hk^2 \right] \\
&= \frac{\partial u}{\partial x}(x_{\frac{1}{2}}, t^{n+\frac{1}{2}}) + \mathcal{O}(h^3) \\
&\quad + \frac{k^3}{48h} \left[-\frac{6}{48}g'''(t^{n+\frac{1}{2}}) - 6e^{(0)} + 6(f'(g(t^{n+\frac{1}{2}})))^{-1}e^{(1)}\frac{h}{k} \right].
\end{aligned} \tag{36}$$

The term $\mathcal{O}(h^3)$ in the second expression results from the interpolation approximation. In order to eliminate the low-order terms, we require

$$\begin{aligned} f'(g(t^{n+\frac{1}{2}}))^{-1}e^{(1)} &= 0, \\ -\frac{6}{48}g'''(t^{n+\frac{1}{2}}) - 6e^{(0)} + 6(f'(g(t^{n+\frac{1}{2}})))^{-1}e^{(1)}\frac{h}{k} &= 0. \end{aligned} \quad (37)$$

Solving the above system of linear equations with respect to $e^{(0)}$ and $e^{(1)}$ leads to

$$\begin{aligned} e^{(0)} &= -\frac{1}{48}g'''(t^n), \\ e^{(1)} &= 0. \end{aligned} \quad (38)$$

Therefore at the intermediate stage $t^{n+\frac{1}{2}}$, the boundary conditions used in the numerical computations are modified as

$$\begin{aligned} g^{n+\frac{1}{2}} &= g(t^{n+\frac{1}{2}}) + e^{(0)}k^3 = g(t^{n+\frac{1}{2}}) - \frac{k^3}{48}g'''(t^{n+\frac{1}{2}}), \\ (g')^{n+\frac{1}{2}} &= g'(t^{n+\frac{1}{2}}). \end{aligned} \quad (39)$$

With the allowance of the accuracy order, $g'''(t^{n+\frac{1}{2}})$ is used in the final result instead of $g'''(t^n)$ to simplify the numerical implementation.

Remark 3.1. *The final intermediate boundary values (39) are consistent with those given in [16] where the author indicates that the boundary values used at the intermediate stage should have the same truncation errors as those in the interior cells.*

3.3. Outflow boundary treatment

In (1), we set $x_{M+\frac{1}{2}} = 1$ as an outflow boundary. Theoretically, no boundary condition is required. However, we have to interpolate it to obtain required values in ghost cells in order to implement the scheme. Take j to be $M+1$ and M in (11). Then \bar{u}_{M+1} , \bar{u}_{M+2} , Δu_{M+1} and Δu_{M+2} are needed. Since the signal propagates out of the computational domain through the boundary $x = 1$, the extrapolation can be used to construct the data in the ghost cells indexed by

$j = M+1, M+2$. Here the extrapolation developed in [19] is briefly summarized.

In order to achieve the fourth-order accuracy, a cubic polynomial is constructed by using the values \bar{u}_{M-3} , \bar{u}_{M-2} , \bar{u}_{M-1} and \bar{u}_M , which is

$$\begin{aligned}
q(x) = & \frac{\bar{u}_M - 3\bar{u}_{M-1} + 3\bar{u}_{M-2} - \bar{u}_{M-3}}{6h^3}(x-1)^3 \\
& + \frac{5\bar{u}_M - 13\bar{u}_{M-1} + 11\bar{u}_{M-2} - 3\bar{u}_{M-3}}{4h^2}(x-1)^2 \\
& + \frac{35\bar{u}_M - 69\bar{u}_{M-1} + 45\bar{u}_{M-2} - 11\bar{u}_{M-3}}{12h}(x-1) \\
& + \frac{25\bar{u}_M - 23\bar{u}_{M-1} + 13\bar{u}_{M-2} - 3\bar{u}_{M-3}}{12}.
\end{aligned} \tag{40}$$

This leads to the values

$$\begin{aligned}
\bar{u}_{M+1} &= 4\bar{u}_M - 6\bar{u}_{M-1} + 4\bar{u}_{M-2} - \bar{u}_{M-3}, \\
\bar{u}_{M+2} &= 10\bar{u}_M - 20\bar{u}_{M-1} + 15\bar{u}_{M-2} - 4\bar{u}_{M-3}, \\
\Delta u_{M+1} &= \frac{26\bar{u}_M - 57\bar{u}_{M-1} + 42\bar{u}_{M-2} - 11\bar{u}_{M-3}}{6}, \\
\Delta u_{M+2} &= \frac{47\bar{u}_M - 114\bar{u}_{M-1} + 93\bar{u}_{M-2} - 26\bar{u}_{M-3}}{6}.
\end{aligned} \tag{41}$$

If there is a discontinuity in either I_{M-3} , I_{M-2} , I_{M-1} or I_M , a WENO-type stencil selection can be used. Details can be found in [20].

4. Boundary treatment for systems

This section turns to investigate numerical boundary treatment for hyperbolic systems. We focus on hyperbolic conservation laws. As far as source terms are included, the corresponding extensions are automatically made. Systems of hyperbolic conservation laws in one dimension read

$$\frac{\partial \mathbf{u}}{\partial t} + \frac{\partial \mathbf{f}(\mathbf{u})}{\partial x} = 0, \tag{42}$$

where \mathbf{u} has m components $\mathbf{u} = (u_1, \dots, u_m)^\top$, $x \in (0, 1)$ and $t > 0$, $\mathbf{f}(\mathbf{u})$ is the associated flux vector function. In this section, all bold letters represent vectors. In contrast with the scalar case in Section 3, the case of systems is

more complicated since the inflow and the outflow signals are coupled. The basic idea of numerical treatments originates from [18, 19]. Inflow signals and outflow signals are separated to be treated using the characteristic decomposition so that the technique of inflow and outflow boundary treatments in Section 3 can be applied, respectively.

Denote by $q^{(k)} := \frac{\partial^k q}{\partial x^k}$ the k -th order spatial derivative of a certain quantity q , $k = 0, 1$, and denote by $\frac{\partial \mathbf{f}(\mathbf{u})}{\partial \mathbf{u}}$ the Jacobian of $\mathbf{f}(\mathbf{u})$. Assume that there are m real eigenvalues of $\frac{\partial \mathbf{f}}{\partial \mathbf{u}}(\mathbf{u}^{(0)})$

$$\lambda_1 \leq \dots \leq \lambda_r \leq 0 < \lambda_{r+1} \leq \dots \leq \lambda_m, \quad (43)$$

and a complete set of corresponding left eigenvectors $\mathbf{L}_i(\mathbf{u}^{(0)})$,

$$\mathbf{L}_i(\mathbf{u}^{(0)})^\top \frac{\partial \mathbf{f}(\mathbf{u}^{(0)})}{\partial \mathbf{u}} = \lambda_i \mathbf{L}_i(\mathbf{u}^{(0)}). \quad (44)$$

Thus there are $m - r$ outgoing signals from the boundary $x = 0$ and the number of boundary conditions should equal to the number of outgoing characteristics, symbolically denoted as

$$B_i(\mathbf{u}(0, t)) = \psi_i(t), \quad i = r + 1, \dots, m. \quad (45)$$

We refer to [8] for details. The similar boundary conditions can be imposed when the right boundary is considered.

In the following part of this section, we first propose the general procedure for the one-dimensional conservation systems and then specify to several examples, including the solid-wall boundary condition for the one-dimensional Euler equations, the subsonic inflow and the subsonic outflow boundary conditions involved in the computations of the nuzzle flow problem. In the last subsection, we extend our boundary treatment to the two-dimensional case by implementing it to the solid-wall boundary condition.

4.1. General framework for numerical boundary conditions

At first, introduce characteristic variables

$$(\bar{w}_i)_j = \mathbf{L}_i \cdot \bar{\mathbf{u}}_j, \quad i = 1, \dots, r, \quad (46)$$

where $\bar{\mathbf{u}}_j$ is the cell average of \mathbf{u} over the cell I_j . Theoretically, $L_i(\mathbf{u}^{(0)})$ should be used here. However in practice, we can use $L_i(\bar{\mathbf{u}}_0)$ in the expression (46) if $L_i(\mathbf{u}^{(0)})$ is not available. Since w_1, \dots, w_r are out-going signals, the extrapolation technique in Subsection 3.3 is applied to obtain $w_i^{(0)}$ and $w_i^{(1)}$ for $i = 1, \dots, r$. For example, as the solution is smooth close to the boundary $x = 0$, we have

$$\begin{aligned} w_i^{(0)} &= \frac{1}{12} \left[-25(\bar{w}_i)_0 + 23(\bar{w}_i)_1 - 13(\bar{w}_i)_2 + 3(\bar{w}_i)_3 \right], \\ w_i^{(1)} &= \frac{1}{12h} \left[-35(\bar{w}_i)_0 + 69(\bar{w}_i)_1 - 45(\bar{w}_i)_2 + 11(\bar{w}_i)_3 \right]. \end{aligned} \quad (47)$$

Then we solve the system

$$\begin{cases} \mathbf{L}_1 \cdot \mathbf{u}^{(0)} = w_1^{(0)}, \dots, \mathbf{L}_r \cdot \mathbf{u}^{(0)} = w_r^{(0)}, \\ B_{r+1}(\mathbf{u}^{(0)}) = \psi_{r+1}(t) + e_{r+1}^{(0)} k^3, \dots, B_m(\mathbf{u}^{(0)}) = \psi_m(t) + e_m^{(0)} k^3 \end{cases} \quad (48)$$

to obtain $\mathbf{u}^{(0)} := \mathbf{u}(0, t)$. Here $w_i^{(0)}$ is obtained by (47). For $i \in \{r+1, \dots, m\}$, $e_i^{(0)} k^3$ is the modification term stated in (38) for ψ_i . According to (39), $e_i^{(0)} = -\frac{1}{48} \psi_i'''(t^{n+\frac{1}{2}})$ at the intermediate time stage $t = t^{n+\frac{1}{2}}$ and $e_i^{(0)} = 0$ at $t = t^n$.

In order to derive $\mathbf{u}^{(1)} := \partial \mathbf{u} / \partial x(0, t)$ near the boundary $x = 0$, we pursue the following manipulation. Take the temporal derivative on the both sides of the boundary conditions in (45)

$$\nabla_{\mathbf{u}} B_i(\mathbf{u}^{(0)})^\top \frac{\partial \mathbf{u}}{\partial t}(0, t) = \psi_i'(t), \quad i = r+1, \dots, m. \quad (49)$$

Then the governing equations (42) are adopted to convert the temporal derivatives to the spatial ones

$$\nabla_{\mathbf{u}} B_i(\mathbf{u}^{(0)})^\top \left[-\frac{\partial \mathbf{f}}{\partial \mathbf{u}}(\mathbf{u}^{(0)}) \frac{\partial \mathbf{u}}{\partial x}(0, t) \right] = \psi_i'(t), \quad i = r+1, \dots, m. \quad (50)$$

Furthermore, we have

$$\mathbf{L}_i(\mathbf{u}^{(0)}) \cdot \mathbf{u}^{(1)} = w_i^{(1)}, \quad i = 1, \dots, r \quad (51)$$

by taking spatial derivatives on the both sides of the first r equations in (48).

Thus we derive the following linear system

$$\begin{cases} \mathbf{L}_1 \cdot \mathbf{u}^{(1)} = w_1^{(1)}, \dots, \mathbf{L}_r \cdot \mathbf{u}^{(1)} = w_r^{(1)} \\ \nabla_{\mathbf{u}} B_{r+1}(\mathbf{u}^{(0)})^\top \frac{\partial \mathbf{f}}{\partial \mathbf{u}}(\mathbf{u}^{(0)}) \mathbf{u}^{(1)} = -\psi'_{r+1}(t), \\ \vdots \\ \nabla_{\mathbf{u}} B_m(\mathbf{u}^{(0)})^\top \frac{\partial \mathbf{f}}{\partial \mathbf{u}}(\mathbf{u}^{(0)}) \mathbf{u}^{(1)} = -\psi'_m(t) \end{cases} \quad (52)$$

with $\mathbf{u}^{(1)}$ as the unknown and $w_i^{(1)}$ in (47).

After obtaining $\mathbf{u}^{(0)} = [u_1^{(0)}, \dots, u_m^{(0)}]^\top$ and $\mathbf{u}^{(1)} = [u_1^{(1)}, \dots, u_m^{(1)}]^\top$ by solving the linear systems (48) and (52), for each pair $u_i^{(0)}$ and $u_i^{(1)}$, $i = 1, \dots, m$, we construct polynomials $p_i^{(r)}$ on the stencils $S_i^{(r)}$, $r = 0, 1, 2$, under the conditions $p_i^{(r)}(0) = u_i^{(0)}$ and $(p_i^{(r)})'(0) = u_i^{(1)}$, as in Subsection 3.1. Then $(\bar{u}_i)_{-1}$, $(\bar{u}_i)_{-2}$, $(\Delta u_i)_{-1}$ and $(\Delta u_i)_{-2}$ are defined as in (25). Finally,

$$\begin{aligned} \bar{\mathbf{u}}_{-1} &= \begin{bmatrix} (\bar{u}_1)_{-1} \\ \vdots \\ (\bar{u}_m)_{-1} \end{bmatrix}, & \bar{\mathbf{u}}_{-2} &= \begin{bmatrix} (\bar{u}_1)_{-2} \\ \vdots \\ (\bar{u}_m)_{-2} \end{bmatrix}, \\ \Delta \mathbf{u}_{-1} &= \begin{bmatrix} (\Delta u_1)_{-1} \\ \vdots \\ (\Delta u_m)_{-1} \end{bmatrix}, & \Delta \mathbf{u}_{-2} &= \begin{bmatrix} (\Delta u_1)_{-2} \\ \vdots \\ (\Delta u_m)_{-2} \end{bmatrix} \end{aligned} \quad (53)$$

will be used in the computation.

4.2. The one-dimensional solid-wall boundary condition

In this subsection, we will implement our boundary treatment (48) and (52) for the solid-wall boundary condition of the one-dimensional compressible Euler

equations,

$$\mathbf{u} = (\rho, \rho v, \rho E)^\top, \quad \mathbf{f}(\mathbf{u}) = (\rho v, \rho v^2 + p, v(\rho E + p))^\top, \quad (54)$$

where ρ, v, p are density, velocity and pressure, $E = \frac{1}{2}v^2 + e$ is the total energy with the internal energy $e = e(p, \rho)$ determined by the equation of state (EOS).

In this paper, we just consider the case of polytropic gases $e = \frac{p}{(\gamma - 1)\rho}$, $\gamma > 1$. Then the Jacobian of the flux function in terms of the conservative variables \mathbf{u} takes

$$\frac{\partial \mathbf{f}}{\partial \mathbf{u}} = \begin{bmatrix} 0 & 1 & 0 \\ \frac{\gamma - 3}{2}v^2 & (3 - \gamma)v & \gamma - 1 \\ \frac{\gamma - 2}{2}v^3 - \frac{1}{\gamma - 1}vc^2 & \frac{3 - 2\gamma}{2}v^2 + \frac{1}{\gamma - 1}c^2 & \gamma v \end{bmatrix}. \quad (55)$$

It has three eigenvalues $\lambda_1 = v - c$, $\lambda_2 = v$ and $\lambda_3 = v + c$, where $c = \sqrt{\gamma p / \rho}$ is the sound speed. The corresponding left eigenvectors are

$$\begin{aligned} \mathbf{L}_1 &= \frac{1}{2c^2} \left[\frac{\gamma - 1}{2}v^2 + vc, -(\gamma - 1)v - c, \gamma - 1 \right]^\top, \\ \mathbf{L}_2 &= -\frac{1}{c^2} \left[\frac{\gamma - 1}{2}v^2 - c^2, -(\gamma - 1)v, \gamma - 1 \right]^\top, \\ \mathbf{L}_3 &= \frac{1}{2c^2} \left[\frac{\gamma - 1}{2}v^2 - vc, -(\gamma - 1)v + c, \gamma - 1 \right]^\top. \end{aligned} \quad (56)$$

Assume that $x = 0$ is a solid wall, on which the flow velocity is zero, $v(0, t) = 0$ which leads to

$$u_2(0, t) = \rho(0, t)v(0, t) = 0. \quad (57)$$

So the system (48), when specified to the current case, is

$$\begin{cases} \mathbf{L}_1 \cdot \mathbf{u}^{(0)} = w_1^{(0)}, \\ \mathbf{L}_2 \cdot \mathbf{u}^{(0)} = w_2^{(0)}, \\ w_2^{(0)} = 0. \end{cases} \quad (58)$$

The modification term in (48) is zero in this and all the following cases since ψ takes a constant value at the boundary and therefore ψ''' is always zero.

Taking temporal derivatives at both sides of $u_2^{(0)} = 0$ and converting the temporal derivatives into spatial ones, we obtain

$$\begin{aligned}
0 &= [0, 1, 0] \frac{\partial \mathbf{f}}{\partial \mathbf{u}}(\mathbf{u}^{(0)}) \mathbf{u}^{(1)} \\
&= \left[\frac{\gamma - 3}{2} (v^{(0)})^2, (3 - \gamma)v^{(0)}, \gamma - 1 \right] \mathbf{u}^{(1)} \\
&= [0, 0, \gamma - 1] \mathbf{u}^{(1)}.
\end{aligned} \tag{59}$$

The last equality comes from the boundary condition $v^{(0)} = 0$. So (52) becomes, for this specific case,

$$\begin{cases} \mathbf{L}_1 \cdot \mathbf{u}^{(1)} = w_1^{(1)}, \\ \mathbf{L}_2 \cdot \mathbf{u}^{(1)} = w_2^{(1)}, \\ [0, 0, \gamma - 1] \mathbf{u}^{(1)} = 0. \end{cases} \tag{60}$$

The numerical example with the solid-wall boundary condition is presented in Example 5 when dealing with the Woodward–Colella problem.

4.3. Inflow and outflow boundary conditions for the nozzle flow

The nozzle flow is ubiquitous in gas dynamics. See [1] and references therein. The nozzle flow is an IBVP for the Euler equations with the geometry effect resulting from the shape of the duct. The governing equations takes the form

$$\frac{\partial}{\partial t} \begin{bmatrix} \rho \\ \rho v \\ \rho E \end{bmatrix} + \frac{\partial}{\partial x} \begin{bmatrix} \rho v \\ \rho v^2 + p \\ v(\rho E + p) \end{bmatrix} = -\frac{A'(x)}{A(x)} \begin{bmatrix} \rho v \\ \rho v^2 \\ v(\rho E + p) \end{bmatrix}, \tag{61}$$

where $A(x)$ is the sectional area of the duct. In Example 6 of the next section, the duct occupies the computational domain $[0, 1]$. The fluid flows into the duct at $x = 0$ and flows out of the duct at $x = 1$. Therefore three kinds of boundary conditions are involved in the computations and they are the subsonic inflow boundary condition, the subsonic outflow boundary condition and the supersonic boundary condition. As for the supersonic out-going flow at $x = 1$, we

can simply extrapolate \mathbf{u} by using the WENO-type extrapolation component-wise.

(I) Subsonic inflow boundary condition. As $|v| < c$ at $x = 0$, the inflow is subsonic. That is, $v - c < 0$, $v + c > v > 0$ at $x = 0$. Then two boundary conditions are required at this end. In our computation, the inflow pressure and the inflow density are given as

$$\begin{aligned} (\gamma - 1)\left[u_3(0, t) - \frac{1}{2} \frac{u_2(0, t)^2}{u_1(0, t)}\right] &= p_{\text{in}}(t), \\ u_1(0, t) &= \rho_{\text{in}}(t). \end{aligned} \quad (62)$$

These two equations as well as $\mathbf{L}_1 \cdot \mathbf{u}^{(0)} = w_1^{(0)}$ lead to the specific form of (48) in this case.

In order to get $\mathbf{u}^{(1)}$, we take temporal derivatives at both sides of (62) to obtain

$$\begin{aligned} & \left[\frac{1}{2}(v^{(0)})^3 - \frac{1}{\gamma - 1}(c^{(0)})^2 v^{(0)}, -(v^{(0)})^2 + \frac{1}{\gamma - 1}(c^{(0)})^2, v^{(0)}\right] \mathbf{u}^{(1)} \\ &= -p'_{\text{in}} - \frac{A'(0)}{A(0)} v^{(0)} (\rho^{(0)} E^{(0)} + p^{(0)}), \\ [0, 1, 0] \mathbf{u}^{(1)} &= -\rho'_{\text{in}} - \frac{A'(0)}{A(0)} \rho^{(0)} v^{(0)}. \end{aligned} \quad (63)$$

Combine them with $\mathbf{L}_1 \cdot \mathbf{u}^{(1)} = w_1^{(1)}$ to get the specific form of (48).

(II) Subsonic outflow boundary condition. At the exit of the nozzle $x = 1$, the out-going flow is subsonic if $v - c < 0$ and $v + c > v > 0$. This means that only the characteristics associated with $v - c$ are impinging onto the exit $x = 1$ from outside of the computational domain. Therefore just one boundary condition is prescribed theoretically at this end. In the conventional treatment, the outflow pressure at the exit is given, denoted by p_{ex} . So the boundary condition is

$$(\gamma - 1) \left[u_3(1, t) - \frac{1}{2} \frac{u_2(1, t)^2}{u_1(1, t)} \right] = p_{\text{ex}}(t). \quad (64)$$

The above equation and $\mathbf{L}_2 \cdot \mathbf{u}^{(0)} = w_2^{(0)}$ and $\mathbf{L}_3 \cdot \mathbf{u}^{(0)} = w_3^{(0)}$ give us the specific form of (48).

Once again, for the linear system of $\mathbf{u}^{(1)}$, take temporal derivatives at both sides of (64) and convert the temporal derivatives to the spatial ones to get

$$\begin{aligned} & \left[\frac{1}{2}(v^{(0)})^3 - \frac{1}{\gamma-1}(c^{(0)})^2 v^{(0)}, -(v^{(0)})^2 + \frac{1}{\gamma-1}(c^{(0)})^2, v^{(0)} \right] \mathbf{u}^{(1)} \\ & = -p'_{\text{ex}} - \frac{A'(1)}{A(1)} v^{(0)} (\rho^{(0)} E^{(0)} + p^{(0)}). \end{aligned} \quad (65)$$

Then, combine it with $\mathbf{L}_2 \cdot \mathbf{u}^{(1)} = w_2^{(1)}$ and $\mathbf{L}_3 \cdot \mathbf{u}^{(1)} = w_3^{(1)}$.

4.4. Solid-wall boundary condition for the two-dimensional Euler equations

In this subsection, we show how this boundary treatment deals with the solid-wall boundary condition of the two-dimensional Euler equations

$$\frac{\partial \mathbf{u}}{\partial t} + \frac{\partial \mathbf{f}(\mathbf{u})}{\partial x} + \frac{\partial \mathbf{g}(\mathbf{u})}{\partial y} = 0 \quad (66)$$

with

$$\mathbf{u} = \begin{bmatrix} \rho \\ \rho v^x \\ \rho v^y \\ \rho E \end{bmatrix}, \quad \mathbf{f}(\mathbf{u}) = \begin{bmatrix} \rho v^x \\ \rho(v^x)^2 + p \\ \rho v^x v^y \\ v^x(\rho E + p) \end{bmatrix}, \quad \mathbf{g}(\mathbf{u}) = \begin{bmatrix} \rho v^y \\ \rho v^x v^y \\ \rho(v^y)^2 + p \\ v^y(\rho E + p) \end{bmatrix}, \quad (67)$$

where $\rho, (v^x, v^y), p$ are density, velocity and pressure, $E = \frac{1}{2}((v^x)^2 + (v^y)^2) + e$ the total energy with the internal energy $e = \frac{1}{\gamma-1} \frac{p}{\rho}$ for polytropic gases.

Consider the computational domain $\Omega = \{(x, y) : x > 0, y \in [y_{\min}, y_{\max}]\}$ with a solid wall $\Gamma = \{(x, y) : x = 0, y \in [y_{\min}, y_{\max}]\}$. The Jacobian of the flux normal to Γ , $\partial \mathbf{f} / \partial \mathbf{u}$, has four eigenvalues $\lambda_1 = v^x - c$, $\lambda_2 = \lambda_3 = v^x$ and $\lambda_4 = v^x + c$ and four associated left eigenvectors $\mathbf{L}_1^x, \mathbf{L}_2^x, \mathbf{L}_3^x$ and \mathbf{L}_4^x .

Along the boundary Γ , we have the solid-wall boundary condition $v^x(0, y, t) = 0$, which give us $u_2^{(0)} = 0$. Combining this with $\mathbf{L}_i^x \cdot \mathbf{u}^{(0)} = w_i^{(0)}$, $i = 1, 2, 3$, will specify the system (48) of $\mathbf{u}^{(0)}$ for the current case.

By taking temporal derivatives at both sides of $u_2^{(0)} = 0$ and converting the temporal derivatives to the spatial ones, one obtains

$$[0, 1, 0, 0] \left(-\frac{\partial \mathbf{f}}{\partial \mathbf{u}}(\mathbf{u}^{(0)}) \frac{\partial \mathbf{u}}{\partial x}(0, y, t) - \frac{\partial \mathbf{g}}{\partial \mathbf{u}}(\mathbf{u}^{(0)}) \frac{\partial \mathbf{u}}{\partial y}(0, y, t) \right) = 0, \quad (68)$$

or

$$[0, 1, 0, 0] \frac{\partial \mathbf{f}}{\partial \mathbf{u}}(\mathbf{u}^{(0)}) \mathbf{u}^{(1)} = -[0, 1, 0, 0] \frac{\partial \mathbf{g}}{\partial \mathbf{u}}(\mathbf{u}^{(0)}) \frac{\partial \mathbf{u}}{\partial y}(0, y, t) = 0. \quad (69)$$

The last equality can be derived from the facts that $u_2^{(0)} = 0$ and that $\frac{\partial u_2}{\partial y}(0, y, t) = 0$ as well as the specific forms of $\partial \mathbf{g} / \partial \mathbf{u}$, $\partial \mathbf{u} / \partial y$ in (67). Combing (69) with $\mathbf{L}_i \cdot \mathbf{u}^{(1)} = w_i^{(1)}$, $i = 1, 2, 3$ leads to the specific form of (52) in this case.

The two-dimensional numerical examples with the solid-wall boundary condition are presented in Examples 7 and 8 in the next section when dealing with the double Mach reflection problem and the forward facing step problem.

5. Numerical examples

All examples displayed in this section are computed using the two-stage fourth-order scheme on Cartesian grids with the GRP solver [2] as the representative of the Lax–Wendroff type flow solvers. The fifth order Hermite-type WENO reconstruction is used for the spatial reconstruction. We denote this scheme by GRP4-HWENO5.

Example 1. Linear scalar equations with smooth solutions. We use a linear equation as the first example to verify the accuracy order of the current boundary treatment. Consider the scalar IBVP (1) with the flux $f(u) = u$. The

initial and the boundary conditions are $u_0(x) = \sin(2\pi x)$ and $g(t) = \sin(-2\pi t)$, respectively. The setting of the initial data and the boundary condition allows the solution to be periodic. The inflow and outflow boundary treatments are applied at $x = 0$ and $x = 1$, respectively.

The CFL number is set to be 0.4. The computation stops at $t = 5$. The numerical errors and orders are shown in Table 5, which confirms that the computation attains the expected order of accuracy.

Table 1: The numerical errors and orders in Example 1.

m	L_1 error	order	L_∞ error	order
40	4.97e-07	4.32	1.75e-06	4.95
80	2.85e-08	4.13	8.64e-08	4.34
160	1.76e-09	4.02	5.66e-09	3.93
320	1.10e-10	4.00	3.60e-10	3.98
640	6.86e-12	4.00	2.27e-11	3.99

Example 2. Nonlinear scalar equations. This example purposes to see the accuracy order for nonlinear equations. Consider the scalar IBVP (1) with the flux $f(u) = (u/2)^2$ and the initial value $u_0(x) = 0.5 + 0.25 \sin(2\pi x)$. The boundary condition $g(t)$ is given to be consistent with the initial value problem in which we periodically extend the initial data to $x \in \mathbb{R}$. At $x = 0$, there are no explicit expressions available for $g(t)$ and its derivatives because of the nonlinearity. However, pointwise values of g could be obtained through the characteristic method and its derivatives can be calculated approximately.

The CFL number is set to be 0.4. The computation stops at $t = 1/3\pi$. For this example, when $0 < t < 1/3\pi$, $x = 0$ is always an inflow boundary while $x = 1$ is always an outflow boundary. Therefore the inflow and outflow boundary treatments are applied at $x = 0$ and $x = 1$, respectively. The numerical errors and accuracy orders in Table 2 shows that the computation reaches the

expected order of accuracy.

Table 2: The numerical errors and orders in Example 2.

m	L_1 error	order	L_∞ error	order
40	6.00e-06	5.15	4.27e-05	4.07
80	1.49e-07	5.33	9.84e-07	5.44
160	7.63e-09	4.29	4.25e-08	4.53
320	4.77e-10	4.00	2.51e-09	4.09
640	2.95e-11	4.01	1.61e-10	3.96

Example 3. Linear systems, Consider the linearized Euler equations

$$\frac{\partial}{\partial t} \begin{bmatrix} \hat{\rho} \\ \hat{v} \\ \hat{p} \end{bmatrix} + \begin{bmatrix} \bar{v} & \bar{\rho} & 0 \\ 0 & \bar{v} & 1/\bar{\rho} \\ 0 & \gamma\bar{p} & \bar{v} \end{bmatrix} \frac{\partial}{\partial x} \begin{bmatrix} \hat{\rho} \\ \hat{v} \\ \hat{p} \end{bmatrix} = 0, \quad x \in (0, 2), \quad t > 0 \quad (70)$$

with the background state $(\bar{\rho}, \bar{v}, \bar{p})$ and the perturbation $(\hat{\rho}, \hat{v}, \hat{p})$, where $\gamma = 1.4$ is the specific heat ratio. The eigenvalues of \bar{A} are $\lambda_1 = \bar{v} - \bar{c}$, $\lambda_2 = \bar{v}$ and $\lambda_3 = \bar{v} + \bar{c}$ with $\bar{c}^2 = \gamma\bar{p}/\bar{\rho}$. In this example, we set $\bar{\rho} = 1.4$, $\bar{v} = 1$ and $\bar{p} = 4$, which makes $\lambda_1 < 0 < \lambda_2 < \lambda_3$. Therefore the subsonic inflow and the subsonic outflow boundary conditions are prescribed at $x = 0$ and $x = 2$, respectively.

This example is designed to make the solution a combination of three sine waves carried by the three characteristics, i.e.

$$\begin{bmatrix} \hat{\rho}(x, t) \\ \hat{v}(x, t) \\ \hat{p}(x, t) \end{bmatrix} = (\mathbf{R}_1, \mathbf{R}_2, \mathbf{R}_3) \begin{bmatrix} \alpha_1 \sin(k_1 \pi (x - (\bar{v} - \bar{c})t)) \\ \alpha_2 \sin(k_2 \pi (x - \bar{v}t)) \\ \alpha_3 \sin(k_3 \pi (x - (\bar{v} + \bar{c})t)) \end{bmatrix}, \quad (71)$$

where k_i and α_i , $i = 1, 2, 3$ are parameters, and

$$\mathbf{R}_1 = \begin{bmatrix} 1 \\ -\frac{\bar{c}}{\bar{\rho}} \\ \bar{c}^2 \end{bmatrix}, \quad \mathbf{R}_2 = \begin{bmatrix} 1 \\ 0 \\ 0 \end{bmatrix}, \quad \mathbf{R}_3 = \begin{bmatrix} 1 \\ \frac{\bar{c}}{\bar{\rho}} \\ \bar{c}^2 \end{bmatrix}. \quad (72)$$

For example, we set $k_1 = 1$, $k_2 = 3$, $k_3 = 2$, $\alpha_1 = 0.1$, $\alpha_2 = -0.1$ and $\alpha_3 = 0.08$. Following the instruction of the fluid dynamics [14], the inflow density $\hat{\rho}(0, t)$ and pressure $\hat{p}(0, t)$ are given at $x = 0$ and the outflow pressure $\hat{p}(2, t)$ is given at $x = 2$. The initial condition is defined by setting $t = 0$.

In the computation, the subsonic inflow and the subsonic outflow boundary treatments are applied at $x = 0$ and $x = 2$, respectively. The CFL condition is 0.4 and the output time is $t = 10$. Table 3 shows the numerical errors and orders.

Table 3: The numerical errors and orders in Example 3.

m	L_1 error	order	L_∞ error	order
40	1.87e-2	-0.12	2.11e-2	0.06
80	8.18e-4	4.52	1.01e-3	4.39
160	4.08e-5	4.33	4.54e-5	4.47
320	2.79e-6	3.87	3.04e-6	3.90
640	1.78e-7	3.97	1.89e-7	4.00

Example 4. Scalar advection equations with discontinuous solutions.

In this example, we verify the capability of our boundary treatment to deal with the discontinuous boundary condition. The same example with similar initial and boundary conditions was used in [19] for the same purpose. Consider the IBVP (1) with the flux to be linear, $f(u) = u$. The initial data is $u_0(x) = \sin(4\pi x)$ and the boundary data is taken as

$$g(t) = \begin{cases} \sin(-4\pi t), & t < 0.25, \\ 0, & 0.25 < t < 0.5, \\ 3, & t > 0.5. \end{cases} \quad (73)$$

The inflow and outflow boundary treatments are applied at $x = 0$ and $x = 1$, respectively. We compare the result in the domain $(0, 1)$ with the exact one in Figure 2. The numerical solution matches the exact solution represented by the

solid line perfectly.

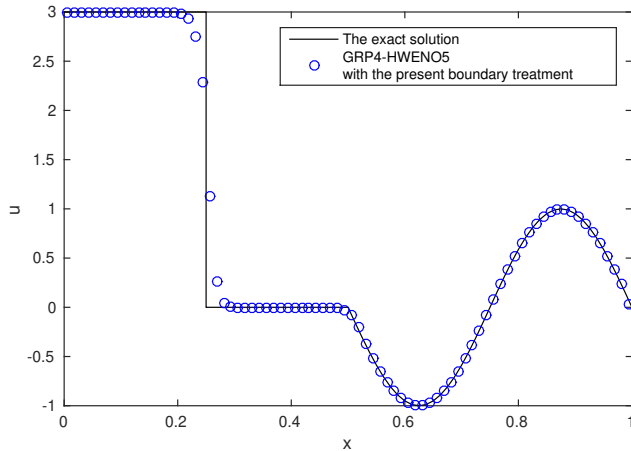


Figure 2: The discontinuous solution in Example 4 with 80 computational cells (circles). The exact solution is shown as a solid curve.

Example 5. The Woodward–Colella problem. This classical example assumes that initially the gas is at rest and ideal with $\gamma = 1.4$ in the computation domain $[0, 1]$, the density is everywhere unit and the pressure is $p = 1000$ for $0 \leq x < 0.1$ and $p = 100$ for $0.9 < x \leq 1.0$, while it is only $p = 0.01$ in $0.1 < x < 0.9$.

The solid-wall boundary condition is prescribed at both ends. Two numerical methods are used to deal with the boundary condition. The first one is the traditional numerical treatment with which we simply symmetrically extend the solution values into the ghost cells. The second one uses the present boundary treatment in the solid-wall case, with which the procedure in Subsections 4.1 and 4.2 are applied. The CFL number is 0.6.

The numerical solutions using both numerical boundary treatments are displayed in Figure 3 at output time $t = 0.038$, in comparison with that using symmetric extension of interior information to the ghost cells. The results are

quite similar.

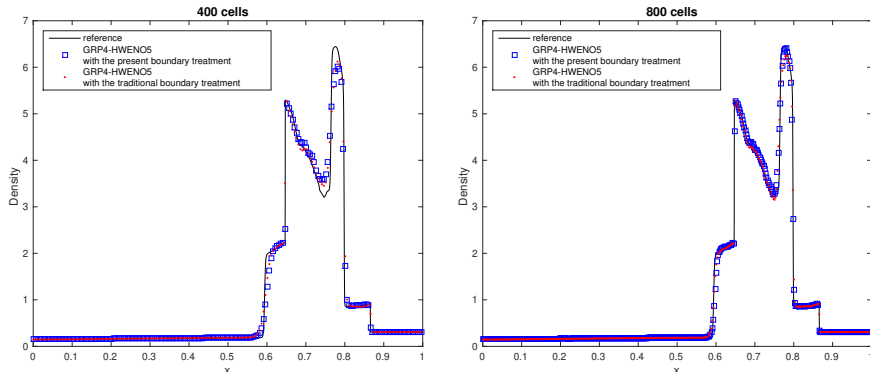


Figure 3: The Woodward–Colella problem Computed with the present boundary treatment (squares) and the conventional reflection boundary condition (dots) with 400 cells (200 are shown, left) and 800 cells (400 are shown, right). The numerical scheme used is the GRP4-HWENO5 scheme. The solid lines are the reference solution computed with 4000 cells.

Example 6. The nozzle flow. The problem of nozzle flow is quasi one-dimensional. A converging-diverging duct occupies the spatial interval $x \in (0, 1)$ and has a smooth cross-sectional area function $A(x)$ given by

$$A(x) = \begin{cases} A_{\text{in}} \exp[-\log(A_{\text{in}}) \sin^2(2\pi x)], & 0 \leq x \leq 0.25, \\ A_{\text{ex}} \exp[-\log(A_{\text{ex}}) \sin^2(\frac{2\pi(1-x)}{3})], & 0.25 \leq x \leq 0.75. \end{cases} \quad (74)$$

The cross-sectional area reaches its minimal value at $x = 0.25$, which is called the throat of the duct. The governing PDEs of the nozzle flow are the Euler equations with the geometric source terms (61). The fluid flows from the left to the right. We set $x = 0$ as the entrance of the duct and $x = 1$ as the exit. The flow in the duct should finally reaches a steady state as the physics indicates.

There are two types of steady states: a smooth steady state and a discontinuous steady state containing a stationary shock. The initial conditions for both

cases take

$$(\rho(x, 0), v(x, 0), p(x, 0)) = \begin{cases} (\rho_0, 0, p_0), & x < 0.25, \\ (\rho_0(p_{\text{ex}}/p_0)^{1/\gamma}, 0, p_{\text{ex}}), & x > 0.25, \end{cases} \quad (75)$$

where ρ_0 and p_0 are parameters, determining if the steady state is smooth or discontinuous.

The smooth steady solution is the isentropic throughout the whole duct, and is expressed as

$$\begin{aligned} \rho(x) &= \rho_0 \left(1 + \frac{\gamma-1}{2} [M(x)]^2 \right)^{-\frac{1}{\gamma-1}}, \\ p(x) &= p_0 \left(1 + \frac{\gamma-1}{2} [M(x)]^2 \right)^{-\frac{\gamma}{\gamma-1}}, \\ v(x) &= M(x) \sqrt{\gamma p(x)/\rho(x)}, \end{aligned} \quad (76)$$

where ρ_0 and p_0 are given parameters and $M(x)$ is determined by the sectional area $A(x)$ through the relation

$$[A(x)]^2 = \frac{1}{[M(x)]^2} \left[\frac{1}{\gamma+1} \left(1 + \frac{\gamma-1}{2} [M(x)]^2 \right) \right]^{(\gamma+1)/(\gamma-1)}. \quad (77)$$

Particularly, we choose $\rho_0 = p_0 = 1$ and $p_{\text{ex}} = 0.0272237$ in our example. See [14]. In this case, the flow is subsonic upstream to the throat and supersonic downstream to the throat. Thus the inflow boundary condition at the entrance $x = 0$ is prescribed as in (62) with,

$$\begin{aligned} p_{\text{in}} &:= p_0 \left(1 + \frac{\gamma-1}{2} [M(0)]^2 \right)^{-\frac{\gamma}{\gamma-1}}, \\ \rho_{\text{in}} &:= \rho_0 \left(1 + \frac{\gamma-1}{2} [M(0)]^2 \right)^{-\frac{1}{\gamma-1}}. \end{aligned} \quad (78)$$

At the exit $x = 1$, the flow is supersonic and no boundary condition is required. The numerical result is displayed in Figure 4 with the current method, using 100 computational cells. The output time is $t = 18$ and the CFL number is 0.6. The solution converges to the expected steady one.

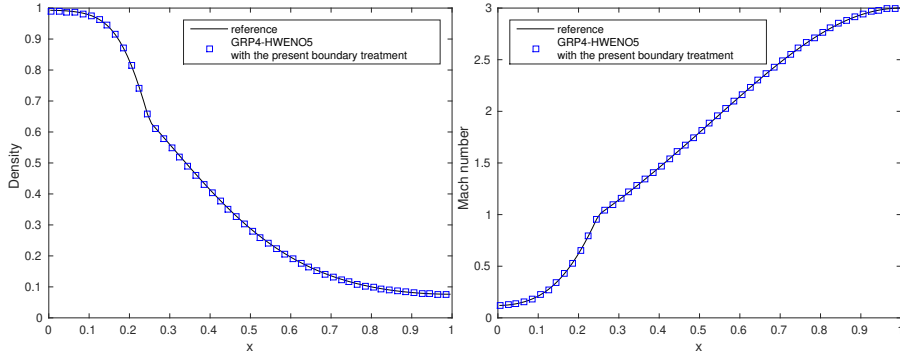


Figure 4: The isentropic flow throughout all the duct computed with the two-stage fourth-order scheme. The density and the Mach number are shown (squares). 100 cells are used. The solid line is the reference solution given by (76).

The other steady solution contains a stationary shock separating two pieces of isentropic solutions defined as in (76) with separate pairs of (ρ_0, p_0) . The shock stands downstream to the throat, and the flow jumps from supersonic to subsonic after passing the shock. The exit $x = 1$ is subsonic for such a case. For this case we set the inflow boundary condition to be (62) and (78) with $\rho_0 = p_0 = 1$ at the entrance $x = 0$ and the outflow boundary condition to be (64) with $p_{\text{ex}} = 0.4$ at the exit $x = 1$. Figure 5 shows the numerical results with 100 computational cells. The output time is $t = 18$ and the CFL number is 0.6. Once again, the solution converges to the expected steady one.

Example 7. The double Mach reflection problem. This is a standard two-dimensional test problem for high resolution schemes. The computational domain for this problem is $[0, 4] \times [0, 1]$, and $[0, 3] \times [0, 1]$ is shown. The reflective wall lies at the bottom of the computational domain starting from $x = \frac{1}{6}$. Initially a right-moving Mach 10 shock is positioned at $x = \frac{1}{6}, y = 0$ and makes a $\frac{\pi}{3}$ angle with the x -axis.

Our computations use both the traditional and the present new numerical boundary treatments to deal with the reflective boundary condition along the

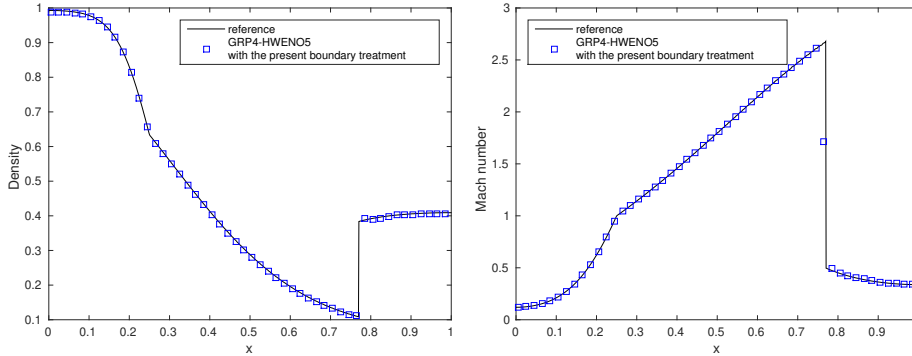


Figure 5: The flow with a steady shock computed with the two-stage fourth-order scheme. The density and the Mach number are shown (squares). 100 cells are used. The solid line is the reference solution given by (76).

wall $\{(x, 0) : x \in [1/6, 4]\}$. For the traditional boundary treatment, we use the symmetrical extension for the ghost cells outside the boundary. For the present new boundary treatment, we apply the procedure in Subsections 4.1 and 4.4. The computations are carried out by the GRP4-HWENO5 scheme with 960×240 grids, using the two numerical boundary treatments. The numerical results are displayed in Figure 6 with 30 contours of the density at time 0.2. The CFL number is 0.6

Example 8. The forward facing step problem. This is also a standard test problem for the two-dimensional computations proposed in [21]. The wind tunnel is 1 length unit wide and 3 length units long. The step is 0.2 length units high and is located 0.6 length units from the left-hand end of the tunnel. The problem is initialized by a unit right-going Mach 3 flow with $(\rho_0, u_0, v_0, p_0) = (1.4, 3, 0, 1)$ in the tunnel. Reflective boundary conditions are applied along the walls of the tunnel.

As in Example 7, both the traditional and the present new boundary treatments are applied to the reflective walls of the tunnel. The numerical results are shown in Figure 7, with 960×320 cells, respectively. The computations stop at

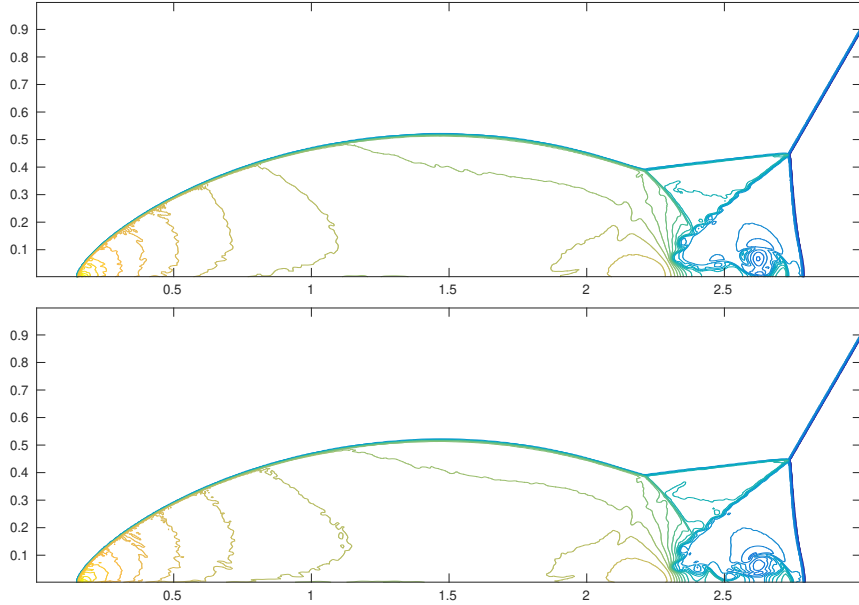


Figure 6: The numerical result of the double mach reflection problem in Example 7 given by the scheme GRP4-HWENO5 combined with the traditional reflection boundary treatment (upper) and the current boundary treatment (lower). The contours of density are shown. 960×240 cells are used.

the time $t = 4$ and the CFL number is 0.6. In both results, the vortices along the slip line can be observed.

6. Discussions

In this paper we provide a method to approximate boundary conditions in order to suit the two-stage fourth order accurate schemes for hyperbolic conservation laws that we proposed earlier [12]. The application is specified to the compressible Euler equations with several commonly-used boundary conditions. We are certainly aware that there are many issues waiting for investigation, such as moving boundary problems, solid wall boundary conditions with curved geometry and small cell problems etc due to the limitation of paper length. All these will be addressed in our forthcoming paper.

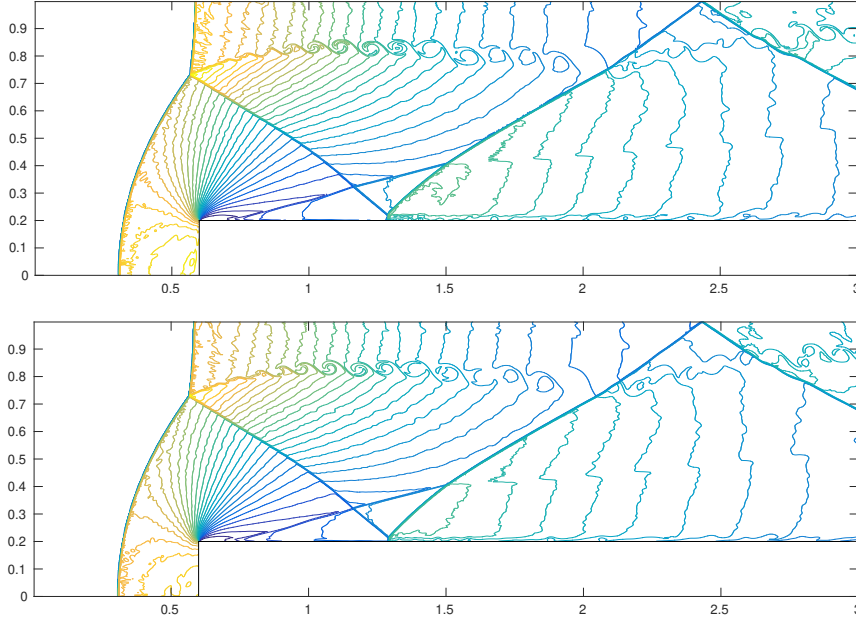


Figure 7: The numerical result of the forward facing step problem in Example 8 given by the scheme GRP4-HWENO5 using the traditional boundary treatment (upper) and the present one (lower). The contours of density are shown. 960×320 cells are used.

Here we would like to emphasize that the inverse Lax-Wendroff approach is fundamental in the sense that the governing equations are effectively adopted to treat the boundary conditions [7, 22, 19, 20, 13]. In the paper the inverse Lax-Wendroff approach is used with the least complexity by taking the advantage of the two-stage method [12]. No successive differentiation of governing equations is made. Nevertheless, the boundary conditions have to be carefully treated at intermediate stages, analogous to any other multi-stage numerical methods.

Of course, just as the fact that the two-stage fourth order method in [12] can be extended to higher order multi-stage method in [15], the current numerical boundary treatment can be extended to much higher order accuracy in a straightforward way. The application to hyperbolic systems beyond the

compressible fluid flows can be treated similarly. We do not want to repeat the technicality from the scientific viewpoint.

Appendix A. The interpolation results in subsection 3.1

This appendix is dedicated to list the interpolation results in Section 3.1. Recall that we assume the left boundary $x = 0$ and $x = 1$ are the inflow and outflow boundaries for the IBVP (1) of the one-dimensional scalar conservation laws, respectively. The stencils are denoted in (19).

Appendix A.1. Cell averages and cell differences

The reconstructed average of u in I_{-1} and I_{-2} on those stencils are:

$$\begin{aligned}
\bar{u}_{-1}^{(2)} &= \frac{1}{4}(-6g + 6h f'(g)^{-1} g' + 11\bar{u}_0 - \bar{u}_1), \\
\bar{u}_{-1}^{(1)} &= h f'(g)^{-1} g' + \bar{u}_0, \\
\bar{u}_{-1}^{(0)} &= g + \frac{1}{2} h f'(g)^{-1} g', \\
\bar{u}_{-2}^{(2)} &= \frac{1}{4}(-90g + 42h f'(g)^{-1} g' + 105\bar{u}_0 - 11\bar{u}_1), \\
\bar{u}_{-2}^{(1)} &= -6gh + 5 f'(g)^{-1} g' + 7\bar{u}_0, \\
\bar{u}_{-2}^{(0)} &= g + \frac{3}{2} h f'(g)^{-1} g'.
\end{aligned} \tag{A.1}$$

The reconstructed x -difference of u in I_{-1} and I_{-2} on those stencils are:

$$\begin{aligned}
\Delta u_{-1}^{(2)} &= \frac{1}{8h}(66g - 34h f'(g)^{-1} g' - 73\bar{u}_0 + 7\bar{u}_1), \\
\Delta u_{-1}^{(1)} &= \frac{1}{2h}(6g - 5h f'(g)^{-1} g' - 6\bar{u}_0), \\
\Delta u_{-1}^{(0)} &= -f'(g)^{-1} g', \\
\Delta u_{-2}^{(2)} &= \frac{1}{8h}(294g - 118h f'(g)^{-1} g' - 331\bar{u}_0 + 37\bar{u}_1), \\
\Delta u_{-2}^{(1)} &= \frac{1}{2h}(18g - 11h f'(g)^{-1} g' - 18\bar{u}_0), \\
\Delta u_{-2}^{(0)} &= -f'(g)^{-1} g'.
\end{aligned} \tag{A.2}$$

Appendix A.2. Smoothness indicators

The smoothness indicators on these stencils are listed as follows,

$$\begin{aligned}\beta^{(2)} &= \frac{1}{80} \left[66516g^2 + 9444(hf'(g)^{-1}g')^2 - 56348f'(g)^{-1}g'h\bar{u}_0 \right. \\ &\quad + 85929\bar{u}_0^2 + 6644f'(g)^{-1}g'h\bar{u}_1 - 20694\bar{u}_0\bar{u}_1 + 1281\bar{u}_1^2 \\ &\quad \left. + 12g(4142f'(g)^{-1}g'h - 12597\bar{u}_0 + 1511\bar{u}_1) \right], \\ \beta^{(1)} &= 48g^2 + 54ghf'(g)^{-1}g' + 16(hf'(g)^{-1}g')^2 \\ &\quad - 96g\bar{u}_0 + 48\bar{u}_0^2 - 54hf'(g)^{-1}g'\bar{u}_0, \\ \beta^{(0)} &= h^2.\end{aligned}\tag{A.3}$$

Acknowledgements

This work is NSFC (nos. 11771054, 11371063) and Foundation of LCP.

References

- [1] M. Ben-Artzi and J. Falcovitz. *Generalized Riemann Problems in Computational Fluid Dynamics*. Cambridge University Press, Cambridge, 2003.
- [2] M. Ben-Artzi, J. Q. Li, and G. Warnecke. A direct Eulerian GRP scheme for compressible fluid flows. *J. Comput. Phys.*, 218:19–43, 2006.
- [3] M. J. Berger, C. Helzel, and R. J. LeVeque. H-box methods for the approximation of hyperbolic conservation laws on irregular grids. *SIAM Journal on Numerical Analysis*, 41:893–918, 2003.
- [4] Mark H. Carpenter, David Gottlieb, Saul Abarbanel, and Wai-Sun Don. The theoretical accuracy of Runge-Kutta time discretizations for the initial boundary value problem: a study of the boundary error. *Math. Comp.*, 52:411–435, 1989.
- [5] H. Forrer and R. Jeltsch. A high-order boundary treatment for Cartesian-grid methods. *Journal of Computational physics*, 140:259–277, 1998.

- [6] C. Helzel, M. J. Berger, and R. J. LeVeque. A high-resolution rotated grid method for conservation laws with embedded geometries. *SIAM Journal on Scientific Computing*, 26:785–809, 2005.
- [7] L. Huang, C.-W. Shu, and M. Zhang. Numerical boundary conditions for the fast sweeping high order weno methods for solving the eikonal equation. *Journal of Computational Mathematics*, 26:336–346, 2008.
- [8] Heinz-Otto Kreiss and Jens Lorenz. *Initial-Boundary Value Problems and the Navier-Stokes Equations*. Academic Press, London, 1989.
- [9] H.-O. Kriess and N.A.Petersson. A second order accurate embedded boundary method for the wave equation with Dirichlet data. *SIAM Journal on Scientific Computing*, 27:1141–1167, 2006.
- [10] H.-O. Kriess, N.A.Petersson, and J. Yström. Difference approximations of the Neumann problem for the second order wave equation. *SIAM Journal on Numerical Analysis*, 42:1292–1323, 2004.
- [11] Lilia Krivodonova and Narsha Berger. High-order accurate implementation of solid wall boundary conditions in curved geometries. *Journal of Computational Physics*, 211:492–512, 2006.
- [12] Jiequan Li and Zhifang Du. A two-stage fourth order temporal discretization for on the Lax-Wendroff type flow solvers, I. Hyperbolic conservation laws. *SIAM, J. Sci. Comput.*, pages A3046–A3069, 2016. 38.
- [13] Tingting Li, C.-W. Shu, and Mengping Zhang. Stability analysis of the inverse lax-wendroff boundary treatment for high order upwind-biased finite difference schemes. *Journal of Computational and Applied Mathematics*, 299:140–158, 2016.
- [14] H. W. Liepmann and A. Roshko. *Elements of Gasdynamics*. Wiley, New York, 1957.

- [15] Liang Pan, Kun Xu, Qibing Li, and Jiequan Li. An efficient and accurate two-stage fourth-order gas-kinetic scheme for the Euler and NavierStokes equations. *Journal of Computational Physics*, 326:197–221, 2016.
- [16] D. Pathria. The correct formulation of intermediate boundary conditions for Runge-Kutta time integration of initial boundary value problems. *SIAM Journal on Scientific Computing*, 18:1255–1266, 1997.
- [17] J. X. Qiu and C.-W. Shu. Hermite WENO schemes and their application as limiters for Runge-Kutta discontinuous Galerkin method: one-dimensional case. *J. Comput. Phys.*, 193:115–135, 2004.
- [18] B. Sjögreen and N.A. Petersson. A Cartesian embedded boundary method for hyperbolic conservation laws. *Communications in Computational Physics*, 2:1199–1219, 2007.
- [19] Sirui Tan and C.-W. Shu. Inverse lax-wendroff procedure for numerical boundary conditions of conservation laws. *J. Comput. Phys.*, 229:8144–8166, 2010.
- [20] Sirui Tan, Cheng Wang, C.-W. Shu, and Jianguo Ning. Efficient implementation of high order inverse lax-wendroff boundary treatment for conservation laws. *J. Comput. Phys.*, 231:2510–2527, 2012.
- [21] P. Woodward and P. Colella. The numerical simulation of two-dimensional fluid flow with strong shocks. *Journal of Computational Physics*, 54:115–173, 1984.
- [22] Tao Xiong, Menping Zhang, Yong-Tao Zhang, and Chi-Wang Shu. Fast sweeping fifth order weno scheme static hamilton-jacobi equations with accurate boundary treatment. *Journal of Scientific Computing*, 45:514–536, 2010.